Research Paper

Preparation of hard carbon/carbon nitride nanocomposites by chemical vapor deposition to reveal the impact of open and closed porosity on sodium storage

Konstantin Schutjajew [a, b], Paolo Giusto [a], Eneli Härk [c], Martin Oschatz [a, b, *]

[a] Department of Colloid Chemistry, Max Planck Institute of Colloids and Interfaces, Am Mühlenberg 1, 14476, Potsdam, Germany
[b] Friedrich-Schiller-University Jena, Institute for Technical Chemistry and Environmental Chemistry, Center for Energy and Environmental Chemistry Jena (CEEC Jena), Philosophenweg 7a, 07743, Jena, Germany
[c] Soft Matter and Functional Materials, Helmholtz-Zentrum Berlin für Materialien und Energie GmbH, Hahn-Meitner-Platz 1, 14109, Berlin, Germany

ARTICLE INFO

ABSTRACT

The sodium-ion battery is a promising successor for the lithium-ion battery. Its energy density is limited by the anode, where sodium ideally is stored at low potentials vs. Na/Na^+. The understanding of the fundamental relationships between material properties and sodium storage is often lagging behind materials development. There is a discord regarding the involvement of so-called "closed pores" in carbons in sodium storage. To investigate their influence, a chemical vapor deposition (CVD) process to deposit polymeric carbon nitride ($p-C_3N_4$) on hard carbon fibres of both, open and closed microporosity, is developed. High storage capacity at a low potential is only possible, when suitable, sealed pores are present. In fibers without notable gas-accessible surface, $p-C_3N_4$ is deposited on the external area, whereas in open-microporous samples the $p-C_3N_4$ phase grows in micropores. Consequently, except for the untreated fibres with closed pores, the composite with a pore gradient along the fibers is the only one in the study that is able to accommodate sodium at low potentials. Neither the remaining graphitic domains, nor the introduced $p-C_3N_4$ are able to accommodate sodium in a quasimetallic state. Finally, not only the sodium storage but also the solid-electrolyte interphase (SEI) build-up is influenced by the additional $p-C_3N_4$ layer.

1. Introduction

The implementation of renewable energy sources has caused a call for grid scale energy storage, which is independent of geographical requirements, operationally safe, and produced from abundant resources. With increasing widespread of renewables in the future, this demand will only rise [1]. The lithium-ion battery (LIB) with its high gravimetric and volumetric energy density would be perfectly suited for this purpose if lithium itself but also related minerals and metal ores were more widely available [2]. In the last decade, considerable research efforts were undertaken to replace scarce lithium by the more available sodium [3]. Wide parts of cell chemistry and compounds are comparable for the two alkaline metals, such as electrolytes, cathode materials and separators. The most striking difference is that graphite, the most widely used anode material in LIBs cannot be used in sodium-ion batteries (SIBs), because contrary to lithium, sodium does not form binary intercalation compounds with graphite [4]. Another carbon modification, so-called "hard carbon", known already from the beginning of alkali-metal battery research, must be employed to store sufficiently high amounts of sodium at low, constant potentials, in order to produce anodes with high energy densities [5,6]. In comparison to graphite, hard carbon is a less ordered carbon allotrope with turbostratically twisted graphene layers forming domains of more or less pronounced graphitic stacking, where the curvature and boundaries of the sheets form internal cavities which remain undetected in gas physisorption, known as internal or closed pores [7–9]. As it was shown in several small-angle X-ray scattering (SAXS) studies, small sodium clusters can be formed inside and stabilized by these internal pores during the sodiation process at a potential close to that of metallic sodium [10,11]. Together with solid-state NMR investigations, this hints at a formal

* Corresponding author. Department of Colloid Chemistry, Max Planck Institute of Colloids and Interfaces, Am Mühlenberg 1, 14476, Potsdam, Germany.
E-mail address: martin.oschatz@uni-jena.de (M. Oschatz).

oxidation state close to zero and a quasimetallic nature of the formed sodium clusters [12–14]. The development of closed-porous materials is subject to chance upon the thermal treatment of suitable hard-carbon precursors [15]. Despite the obvious prospect in the targeted preparation of closed porous carbons, their synthesis with control over the structure was so far demonstrated only a few times in literature [16,17]. From a general point of view there are two evident approaches to the introduction of closed porosity into carbons. The first one is the direct synthesis from thoughtfully chosen starting materials, with or without the use of templates or pore-formation additives. The second, more controllable method is the post synthetic closing of open porous materials by an external coating. Once a protocol for such a coating procedure is established, the impact of different pore structures, volumes, and geometries can be studied. For the application in sodium storage, the ideal coating layer should be not permeable for electrolyte molecules and counter ions, but simultaneously provide a sufficient ionic conductivity for Na^+-ions. The film should also be an electrical insulator, in order to prevent excessive and uncontrolled solid-electrolyte interphase formation through decomposition of electrolyte, thus providing a mechanically and chemically stable, artificial SEI. In this context, polymeric carbon nitride (p-C_3N_4) stands out due to its high flexibility, thermal stability and tunable conductivity and is therefore promising for the application as a pore closing as well as SEI-forming substance [18,19]. The possibility to form dense and homogenous p-C_3N_4 films on different planar substrates by chemical vapor deposition (CVD) was recently explored and demonstrated by Giusto et al. [20,21] Based on these findings, we investigated the influence of a porous carbon structure on the growth of p-C_3N_4, by performing CVD on hard carbon cloth of different porosity and within this scope shed some light on the gas diffusion dynamics during the CVD process. We further investigated the relations between the structure of the coated carbon fibres and the sodium storage properties in SIB anodes. A detailed gas-physisorption and SAXS study reveals that in carbons of a high degree of activation and a pore radius above a certain threshold, the deposition mode shifts from surface coverage towards bulk pore filling. In contrast, successful generation of closed porosity can be observed in moderately activated carbons. Most importantly, in the electrochemical analysis of the materials the effect of artificial pore closure is manifested in a voltage plateau during both, sodiation and desodiation. Starting with a material with virtually no plateau capacity, 54 mAh g^{-1} of sodium can be reversibly stored at a low potential below 300 mV vs. Na/Na^+ in the respective carbon/p-C_3N_4 nanocomposite. Finally, a decrease of first-cycle capacity and therefore a successful action of the p-C_3N_4 layer as an insulating protective film is demonstrated. This proves the viability of the method not only for transforming accessible surface area into closed porosity, which can serve as nucleation point and stabilizing structure for sodium clusters, but also for the generation of a homogenous, artificial SEI-layer.

2. Materials and methods

2.1. Materials preparation

Commercially available carbon cloths (Kynol 5092-CC, -ACC10, and -ACC20) were purchased from Kynol Europa GmbH, Hamburg. Melamine (99%) was obtained from Sigma Aldrich. Prior to each CVD treatment, the carbon cloths were treated in an oxygen plasma cleaner (Harrick PDC-32G-2) at 150 W power for 10 min at a pressure of 0.5 mbar. Plasma treated samples are denoted with "Plasma" as a suffix. Hard carbon/carbon nitride nanocomposites were prepared in a tubular oven with two heating zones (planar-GROW-3S-OS CVD System for Organic Semiconductor, planarTECH)

with a 3 in. quartz tube. In a typical recipe, 5 g of melamine are placed in an in-house-made boat upstream, with the target substrate placed vertically downstream on a quartz holder. The melamine was completely sublimed at 300 °C and p-C_3N_4 was deposited at 550 °C on the target substrate surface. The process was carried out at low pressure (10 Torr) and with N_2 as a gas carrier (50 sccm). After the deposition, the samples were cooled down naturally before collection [20]. The mass gain after CVD was 5% for 5092-CC, 10% for 5092-ACC10, and 45% for 5092-ACC20. Carbon/carbon nitride nanocomposites bear the name of their parent carbon together with the suffix "C_3N_4".

2.2. Structural characterization

N_2 and CO_2 sorption experiments were carried out on a Vapor200C gas sorption analyser at −186 °C and 0 °C, respectively. Before each measurement, the samples were outgassed under vacuum at 150 °C for at least 20 h. Specific surface areas were calculated by the multipoint BET method and the total pore volume was determined at $p/p_0 = 0.99$. Quenched solid density functional theory (QSDFT, for N_2 at 77 K on carbon surfaces with slit/cylindrical pores) on the adsorption branch of the isotherms was used to calculate pore size distributions, pore volumes as well as surface areas of the materials [22,23]. Combustive elemental analysis (EA) was performed on a vario MICRO elemental analyser by Elementar. Thermogravimetric analyses (TGA) were measured using a Netsch TG 209 F1 Libra in a temperature range between room temperature and 1000 °C in platinum crucibles under N_2 and synthetic air atmospheres. Powder X-ray diffraction patterns were acquired on a Bruker D8 in Bragg-Brentano geometry in a 2Θ range of 10–70° with a step size of 0.03° using Cu$_{K\alpha}$ ($\lambda = 0.154$ nm) radiation. The samples were positioned on a horizontal silicon single crystal sample holder. Small-angle X-ray scattering patterns were recorded on a Bruker Nanostar 2 device using Cu$_{K\alpha}$ ($\lambda = 0.15418$ nm) radiation in a sample-detector distance of 28.90 cm. The focal spot of the beam has a diameter of 115 μm. The samples were ground to powders and filled into borosilicate capillaries of 1.5 mm diameter. The data was reduced to dimensions of absolute scattering cross-sections following the method described by Dreiss et al. [24], using water as a primary calibration standard. Additionally, the curves were normalised to the filling density and the amount of the sample in the beam. The fiber morphology was analyzed by scanning electron microscopy (SEM) on a Zeiss Leo Gemini 1550 microscope at 3 kV acceleration voltage. Energy dispersive X-ray spectroscopy (EDX) was performed on a Phenom ProX desktop SEM device using 15 kV acceleration voltage. The samples were prepared by cutting isolated filaments and placing them on vertical Al-holders with their cross-section facing the beam. Raman spectra were measured on a confocal Raman microscope (inVia, Renishaw) using laser radiation of 532 nm wavelength and 5 mW power in an energy range between 500 and 3600 cm^{-1}, scanning 5 times.

2.3. Electrochemical characterization

The carbon cloths were fabricated into electrodes by doctor blading of ground carbon cloth. The cloths were ground in a motorized mortar (Fritsch Pulverisette 2) for 10 min, to obtain a fine powder. In a typical batch, 90 mg of the ground active material was combined with 5 mg of conductive carbon black (Super C65, Timical) and 125 μl of a solution of carboxymethylcellulose (CMC, DuPont, Walocel CRT 2000 PA, 2 mg ml^{-1}), so that 5 mg of CMC were in the ink. The mixture was stirred to homogeneity in an agate mortar and then coated onto a copper foil (99.8%, Alfa Aesar) using a doctor blade at 100 μm wet film thickness at 30 mm s^{-1}. The sheets were transferred into a vacuum oven and dried at 70 °C and

10^{-2} mbar overnight. In this way, an area loading of 1.9–2.5 mg cm^{-2} was achieved, depending mainly on the filling density of the active material. For half-cell tests, discs of 10 mm diameter were punched from the electrode sheets. Half cells were assembled in a two-electrode setup using Teflon-Swagelok type cells, and 200 μl of a 1 M solution of NaPF$_6$ in a 6:4 v/v mixture of ethylene carbonate and diethyl carbonate as the electrolyte. Sodium metal discs served as both, the counter and reference electrode and a Whatman GF/C glass fibre filter was used as the separator. Potentials are referred to as against Na/Na$^+$, unless stated otherwise. In order to ensure comparability to other systems, the current density is applied with respect to the theoretical capacity of a Li-graphite anode (C$_{372}$ = 372 mAh g^{-1}), so that 1 C equals 372 mA g^{-1}. Characterization by charge-discharge measurements was carried out in two steps. First, the bulk sodium plating capacity of the material was determined, by cycling the cell in a voltage range of 2.5−0.002 V, alleviating the lower voltage limit in favor of an intentionally exaggerated, arbitrary capacity limit of 372 mAh g^{-1} in a final cycle. The capacity, at which a voltage minimum was observed is regarded as the maximum sodiation capacity, beyond which metallic sodium is formed [25]. Additionally, the reversible desodiation capacity was measured in the next cycle. In a second step, the materials were galvanostatically sodiated and desodiated with the reversible capacity determined in the previous step set as the capacity limit instead of the voltage limit.

Cyclic voltammetry (CV) was measured in a voltage range of 2.5 to 0.0 V and 2.5 to −0.1 V. Before the actual CV experiment, the cell was cycled in a range of 2.8−3.0 V at increasing scan rates.

3. Results and discussion

3.1. Structural characterization

Carbon materials can be conveniently classified according to their ability to form a graphitic structure upon being subjected to sufficiently high temperatures. Those, capable of transformation into graphite, but carbonized below their graphitization temperature are usually termed soft carbons. These materials are typically fully turbostratic, and also contain defects, causing a certain extent of curvature and tilt [7]. On the other hand, non-graphitizing, or hard carbons are obtained from the carbonization of precursors exhibiting high degrees of cross-linking before and during temperature treatment, which therefore do not develop a long-range order, even after treatment at high temperatures. Instead, regions of several stacked graphene layers alternate with regions where the sheets dilate, forming internal voids. These structural features have been identified as the loci of quasimetallic sodium cluster formation at low potentials in SIB anodes and their presence is key to efficient sodium storage [10,14,26,27]. Among a plethora of possible precursors, phenolic resins are well suited, due to their tuneable microstructure, scalability, and low price [15]. For the present study, carbonized novoloid fiber cloths produced by Kynol Europa GmbH were chosen, as they show reasonable reversible sodiation characteristics, a homogenous, fibrous texture, and narrowly distributed microporosity in case of the activated cloths. Most importantly, the free-standing, textile appearance enables the homogenous growth of p-C$_3$N$_4$ on the substrate within a stationary tube CVD system, contrary to preliminary experiments on different carbon powders. Internally porous Kynol 5092-CC, with virtually no gas-accessible surface area was treated as well as microporous samples Kynol 5092-ACC10 and -ACC20, which were activated in a CO$_2$ stream to different degrees by the manufacturer. In order to achieve a homogenous deposition of p-C$_3$N$_4$ on the carbon surface, the as-received fibers underwent an oxygen plasma etching step in order to activate the surface for the further CVD treatment. The

conditions were chosen according to insights from previous works in a manner, that no significant weight loss due to burning of the carbon skeleton occurred [28]. To rule out effects from this additional pre-treatment, plasma-etched samples were structurally characterized together with the pristine samples and the nanocomposites. Thermal analysis techniques such as TGA and EA can serve as important sources of first insights on the elemental composition of the materials and provide information of the ratio of p-C$_3$N$_4$ to carbon substrate and therefore the results from thermogravimetric analysis under nitrogen, as well as synthetic air atmosphere, are presented in Fig. 1.

The pristine, as well as plasma-etched carbons lose only a few percent of mass under nitrogen atmosphere up to temperatures of 1000 °C, as shown in Fig. 1a), c), and e). Besides an initial mass loss at temperatures below 100 °C, which is due to desorption of adsorbed gases and water and which all samples have in common, a main mass loss signal is observed at 550 °C. This can be clearly assigned to the beginning thermal decomposition of p-C$_3$N$_4$. At this temperature 5092-CC-C$_3$N$_4$ loses about 1% and 5092-ACC10-C$_3$N$_4$ about 2% of their respective mass, while the most microporous carbon fiber sample (5092-ACC20-C$_3$N$_4$) shows a mass loss of 25%. A constant mass loss is observed upon exceeding the temperature of 550 °C, which continues well until 1000 °C. The reason for this behavior is that carbon nitride undergoes an equilibrium decomposition starting at approximately 550 °C, during which different, gaseous carbon-nitrogen species are formed. These compounds can further react with themselves as well as with the substrate, causing a continuous mass loss, especially in samples derived from highly microporous substrates.

The TGA results under N$_2$ are supported by elemental analyses, which are summarized in Table SI1. The nitrogen content serves as a measure for the amount of carbon nitride deposited on the fibers. The N-content increases with the porosity of the substrate and equals 0.64 wt% in 5092-CC-C$_3$N$_4$, 5.13 wt% in -ACC10-C$_3$N$_4$, and finally reaches 20.95 wt% in -ACC20-C$_3$N$_4$. Thermal analysis under synthetic air atmosphere, as presented in Fig. 1b), d), and f) shows one prominent combustion peak with an onset around 650 °C and a maximum at 850 °C in 5092-CC-derived samples. These values are remarkably high compared to those of composites prepared from activated carbon samples and considering the low amount of deposited p-C$_3$N$_4$ are mainly due to the relatively high degree of order in the carbon lattice of the non-activated sample. Pristine and plasma-etched activated carbons begin to lose mass already at 500 °C, while the combustion of the related carbon/carbon nitride composites is retained by about 50 °C. The similar full width at half maximum of the differential mass loss peak in CVD treated samples as in untreated ones indicates a simultaneous decomposition of the carbon substrate together with the grown p-C$_3$N$_4$ phase. It therefore underlines the formation of a homogenous nanocomposite.

Scanning electron micrographs, exemplarily shown for materials derived from Kynol 5092-ACC20 in Fig. 2 portray a similar picture about the development of the morphology of the intermediates during the synthesis of carbon/carbon nitride composites, presented in Figures S1 and S2. All the samples consist of fibers with a diameter of about 10 μm, where the as-received samples exhibit a smooth but inhomogeneous surface with seemingly adsorbed smaller particles. After plasma-etching, the fibers' surface is free from secondary grains and particles. On a higher magnification level, the fibers appear rough and feature crevices sized in the range of tens to hundreds of nanometers all over their surface. This circumstance vividly demonstrates the purpose of plasma activation before any CVD run, as it enables the reactive gas to enter the entire fiber and to grow an even film. After CVD a new structure with a texture different from the parent material can be identified on the surface of each material.
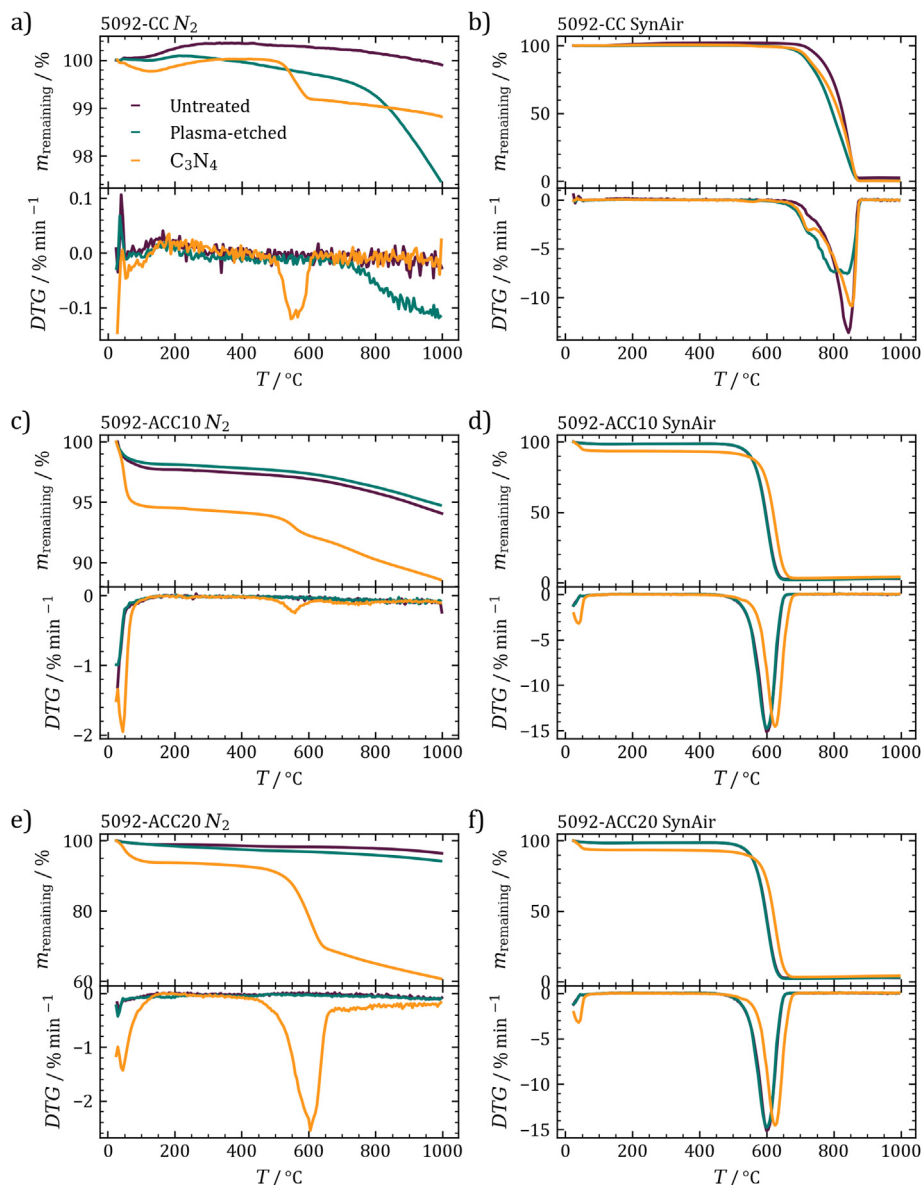
Fig. 1. Thermogravimetric analysis of the materials. a), c), and e) in N₂, b), d), and f) in synthetic air atmosphere, respectively. The upper panel shows a relative residual mass (residue), lower panel shows a differential mass loss (DTG). (A colour version of this figure can be viewed online.)

Insights about the chemical nature of the newly formed layer as well as the carbon underneath can be obtained from Raman spectroscopy. The background-corrected spectra together with fitted bands are shown for untreated materials and carbon/carbon nitride composites in Fig. 3. Plasma treatment does not significantly alter the carbon nanostructure, as can be seen in Fig. S3. All spectra are characterized by features typical of disordered carbonaceous materials, mainly the D-band at 1340 cm^{-1} arising from the breathing mode of carbon six rings at defect sites, the G-band at 1600 cm^{-1} due to in-plane bond stretching vibrations of sp^2 hybridized carbon atoms, and their respective overtones between 2500 and 3500 cm^{-1} [29]. Varying contributions of *trans*-polyacetylene (TPA) vibrations and A-modes due to amorphous carbon regions are found, depending on the activation degree and the presence of p-C₃N₄ in the sample [30,31]. The spectrum of 5092-CC shows sharp D- and G-bands with a shoulder peak at 1124 cm^{-1}. This indicates a highly ordered, sp^2-rich, graphitic structure [29]. From the absence of an A-mode between the D- and G-bands it follows, that the

content of point defects or heteroatoms is low in the carbon fibers [32,33]. Overtone bands can be clearly distinguished, with the 2D4-band at 2476 cm^{-1}, the 2D1-band at 2685 cm^{-1}, the 2D1+G band at 2935 cm^{-1}, and the 2D2-band at 2685 cm^{-1} [34]. Upon CO₂ activation in samples 5092-ACC10 and -20 particularly the D-band but also the G-band broaden and the overtones become less well distinguishable, as well. This is an expected transition of the carbon nanostructure when a highly ordered material is transferred to more disordered, porous carbon.

The decrease of the I_D/I_G-ratio, see Table S2, together with the occurrence of a stronger A-band indicate the decreasing extent of graphitic regions together with the introduction of interstitial sp^3-domains or point defects, such as five- and seven-rings into the carbon framework [31,33]. The impact of p-C₃N₄ deposition onto the material is merely manifested in an increase of the background absorption between the D- and G-bands, which can hardly be reduced to singular bands [35,36]. However, such an increased background signal can be found at the previously discussed
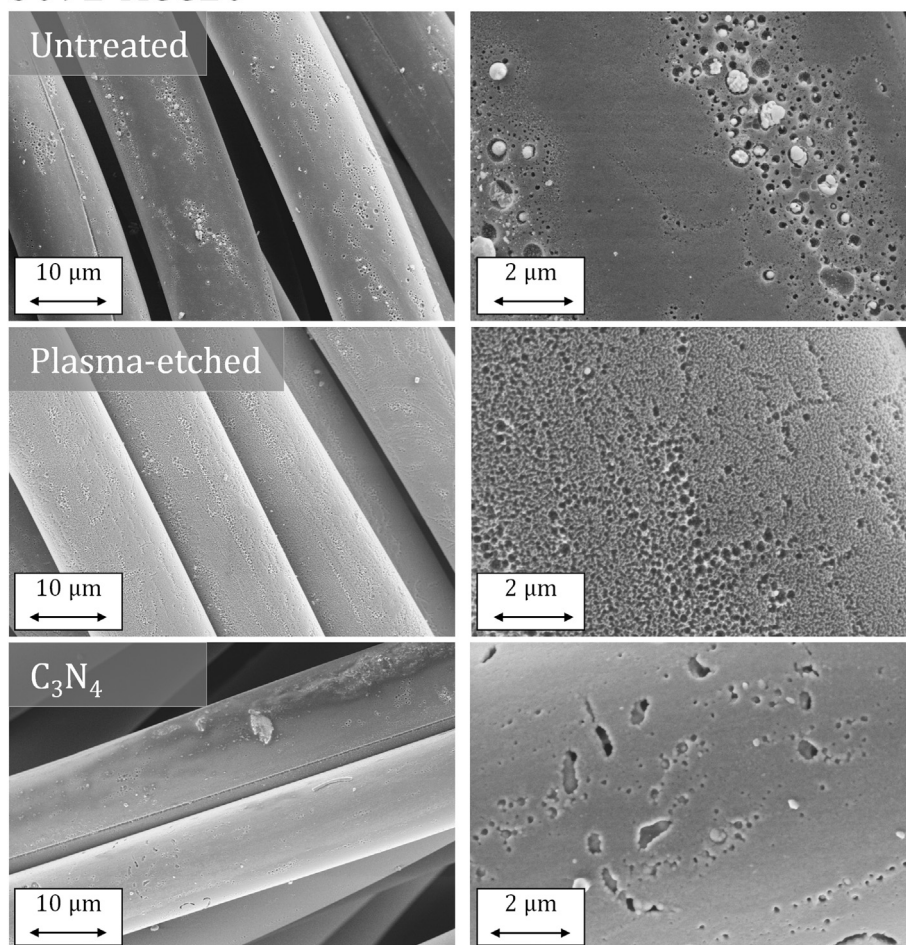
5092-ACC20

Fig. 2. SEM images of Kynol 5092-ACC20 as received (upper panels), plasma etched (middle panels), and after CVD (lower panels).

positions in each sample. The background is most pronounced in 5092-ACC20-C_3N_4, well in line with the high amount of p-C_3N_4 grown on this substrate.

XRD-patterns of untreated Kynol 5092-CC, as presented in Fig. S4, reveal two broad signals at 25° (002) and at 44° (100), which is typical of a hard carbon material. The reflex at the (100) lattice plane is present in all three untreated carbons, while the (002) reflex, originating from diffraction at the interlayer distance of two graphene layers only occurs in Kynol 5092-CC, indicating the existence of rather large graphitic crystallites in this material. Upon depositing p-C_3N_4, the region between 20° and 30° is dominated by diffraction at the (002) plane, indicating stacked layers of carbon nitride formed at the fiber surface.

In order to investigate how deeply the p-C_3N_4 phase propagated into the carbon fibers, single fibers were separated from the cloth and cut along their cross-section. EDX line scans were then measured to determine the radial distribution of carbon and nitrogen. SEM-Figures and the respective line scans are presented in Fig. 4.

The main difference is obviously the gradient in the nitrogen content along the cross-section of the fibers. As the distinction between carbon and nitrogen is difficult from EDX in general, information from EA must be considered in the analysis of this graph. It is known from EA, that 5092-CC-C_3N_4 consists of carbon to more than 99%, yet the EDX-line scan indicates a constant presence of approximately 17% nitrogen. Therefore, this value can be viewed as

a baseline or blind value and the evaluation must be focused on the gradient of the respective element distribution. In 5092-ACC10-C_3N_4 the nitrogen content increases only in the outer 20% of the sample radius and in the remaining central part of the fiber stays very close to the "background" value known from 5092-CC. Finally, 5092-ACC20-C_3N_4 contains up to 36 wt% of nitrogen, according to EDX, even in the center of the fiber, hence clearly indicating the diffusion of the reactive gas throughout the entire sample, contrary to 5092-ACC10-C_3N_4, where the pores in the center are most likely too narrow. Although it would be of highest interest to study the materials at higher levels of magnification and resolution, the samples are ill-suited for transmission electron microscopy, as the fibers are too thick and cutting them would result in a loss of structural integrity of the material.

Additional important insights into the deposition mode, the extent of pore filling and the presence of both, closed and gas-accessible porosity, are obtained by a set of analysis of SAXS patterns and gas-physisorption isotherms independently. SAXS is sensitive to the scattering contrast between vacuum (pores) and condensed matter throughout the entire sample, therefore it can also detect surface area provided by closed pores. Meanwhile, probe gases in sorption experiments obviously only can enter pores with entrances that are larger than their kinetic diameter. N_2 physisorption isotherms are depicted in Fig. 5 a), c), and e), the respective differential and cumulative pore size distributions in Fig. 5 b), d), and f), and the derived numbers in Fig. S5.
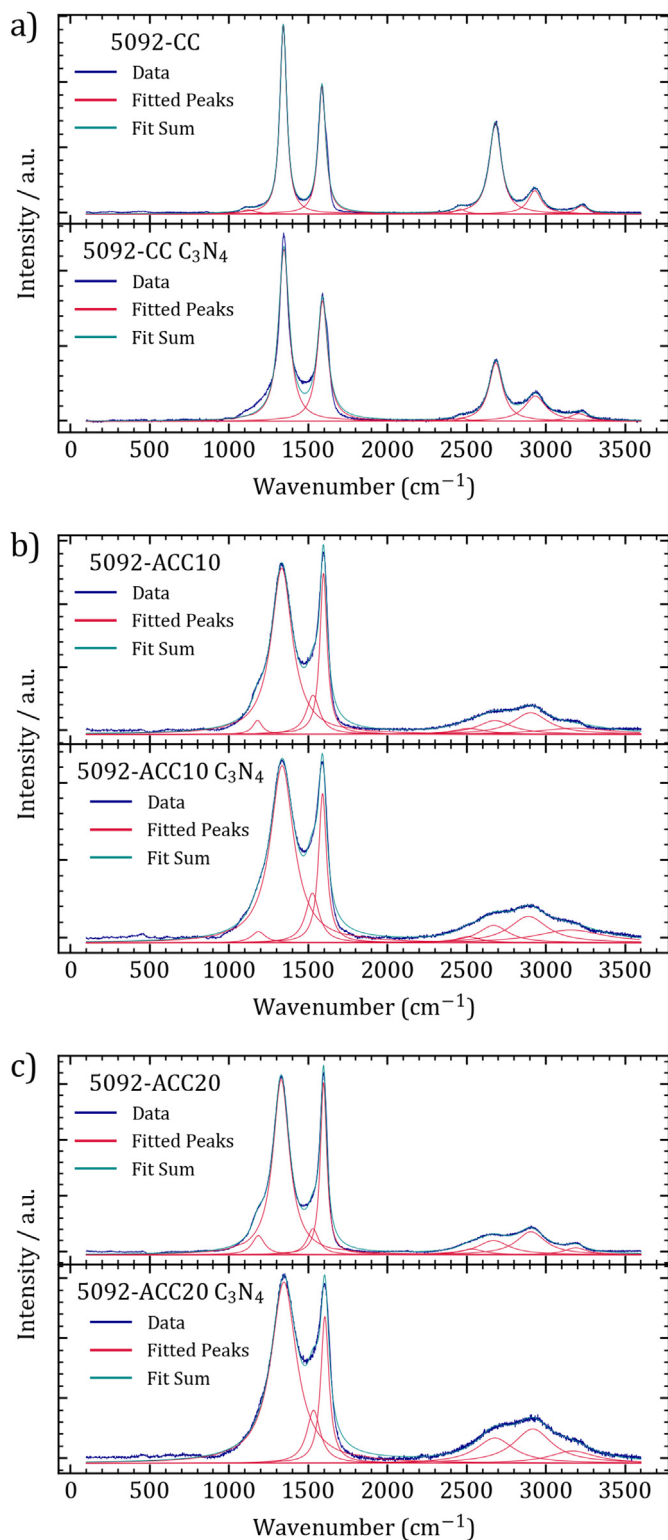
does not affect the total amount of gas adsorbed, but the uptake rather happens at higher relative pressures. The carbon nitride composite from 5092-CC shows a higher uptake of adsorptive and the disappearance of an inflection point in the isotherm, indicating an impeded interaction with the adsorbent surface and clustering of the adsorbate around sites of higher affinity. This effect can be ascribed to the impact of a carbon nitride film on the fiber surface. Nevertheless, the surface areas of all 5092-CC-derived materials are lower than 24 m^2g^{-1} according to DFT. Kynols 5092-ACC10, untreated as well as plasma-etched and CVD-treated, show type I isotherms with rather sharp inflections at the saturation plateau. This is indicative of a highly microporous material with narrow pores, as it is also supported by DFT pore size distributions. The major amount of pore volume is provided by pores smaller than 1 nm. Plasma cleaning slightly increases the surface area from 897 m^2g^{-1} to 1037 m^2g^{-1} as well as the pore volume from 0.324 cm^3g^{-1} to 0.407 cm^3g^{-1}. From the cumulative pore size distribution plot, it becomes evident, that particularly the volume related to smaller micropores as well as the external surface area vanishes. One should keep in mind that a significant amount of pore volume, smaller than the kinetic radius of N_2 might be neglected in this method, therefore, CO_2 sorption measured at 273 K shown in Fig. S6 produces isotherms of similar total gas uptake and inflection for pristine, plasma-activated, and CVD treated Kynol 5092-ACC10. Considering the smaller kinetic diameter of CO_2 and its higher diffusivity at 273 K these results reveal that a part of the ultra-micropores of ACC10 are too small to be accessible to N_2 at cryogenic temperatures as well as to the reactive species during the CVD process and therefore remain unaffected by both, plasma-etching and CVD. CVD causes the greatest change in Kynol 5092-ACC20. While basically identical isotherms are measured before and after plasma-etching, its carbon/carbon nitride composite shows no significant surface area. Considering the pore volume before CVD, which equals to 0.761 cm^3g^{-1}, and assuming a density of the carbon nitride phase of 2 $g\,cm^{-3}$ one would expect a mass increase of more than 150% after CVD if all pores were filled. As the mass gain is lower according to the yield as well as thermal analyses, either an incomplete pore filling or a lower density of the deposited film must be the cause. A plausible explanation is that the reactive gas in the CVD process is likely larger than an N_2 molecule and therefore does not reach some of the smallest micropores. Also, at a temperature of 550 °C, as it is the case in the CVD oven, diffusion stands in direct competition with the surface reaction and subsequent deposition, which hinders the p-C_3N_4 phase from entering some share of the ultramicropores. Therefore, the generation of a "pore size gradient", during CO_2 activation stands to reason, which is supported by physisorption and EDX-line scan measurements. The highly dynamic equilibrium of carbon nitrides in the gas phase could also give rise to nitrogen-doping in the smaller micropores rather than growth of a carbon nitride phase, which to some extent explains why in SEM/EDX line scans the distribution of a significant content of nitrogen is measured even in the fiber bulk. However, the N-contents of 10 wt% or even more than 30 wt% would be suspiciously high for ordinary N-doping. Under the reasonable assumption that the porosity in the carbon is present already in the untreated 5092-ACC20 sample and the reactive intermediates can only reach such open porosity, excluding any solid-state diffusion effects of nitrogen through the carbon framework, it finally stands to notice that by growing a p-C_3N_4 on a porous carbon the distribution of the pore system of the substrate can be nicely visualized, which could be of some use in research on porous materials from an academic point of view.

The SAXS patterns obtained for Kynol samples that accommodate the knee-shaped profiles at $q = 1$ nm^{-1} for unactivated 5092-CC and around 2.5 nm^{-1} for Kynol 5092-ACC10, and -ACC20, were

Fig. 3. Background corrected Raman spectra of untreated carbon fibers and carbon/carbon nitride nanocomposites with fitted bands and fit sum. (A colour version of this figure can be viewed online.)

Kynol 5092-CC before and after plasma treatment shows a type II isotherm with low gas-uptake, indicating unrestricted monolayer-multilayer adsorption. This is in agreement with the non-porous, fibrous structure of the materials [37]. Plasma-etching
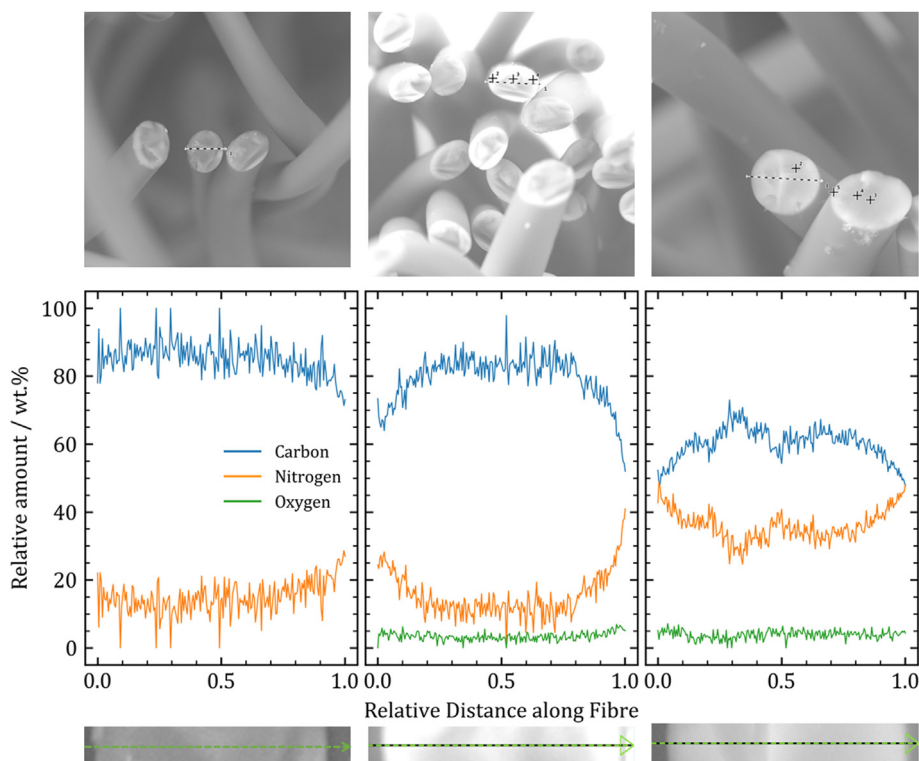
Fig. 4. SEM images of carbon fibres after CVD (top panel), elemental composition along with line scan (lower panel) with magnified SEM image of linescan at x-axis. (A colour version of this figure can be viewed online.)

similar to the patterns presented in the literature, indicating the presence of the microporous structure (Fig. S9 a-c) [10,11]. A model-free approach introduced in the late 1960s by Schiller and Mering [38] followed by Perret and Ruland's [39—42] works was used to analyze the SAXS scattering patterns of ground untreated, plasma treated Kynols and Kynol/carbon nitride nanocomposites (Fig. S7 a-c). For a detailed description of theory and analysis, the reader is referred to refs. [43,44]. In general, the scattering cross-section is a superposition of two different, statistically independent scattering contributions (SI eq. 2). After removal of a fluctuation scattering due to finite layer size and lateral imperfections of the carbon layers (SI eqs. 3 and 4), the ideal two-phase system (scattering of pores in carbon matrix) can be evaluated. Additionally, for samples containing p-C_3N_4, the scattering vector independent 3D density fluctuations of an amorphous phase of p-C_3N_4 was accounted for by subtracting the mass-weighted scattering of previously measured bulk p-C_3N_4 (SI eq. 2a). As the simple subtraction procedure indicates, these scattering contributions superimpose and therefore p-C_3N_4 can be viewed as a statistically independent phase grown on the carbon. All corrected scattering patterns show the classical asymptotic q^{-4}-behaviour, as shown in Fig. SI9 d-f. Structural parameters derived from SAXS are collected in Table S3. Unactivated 5092-CC shows an exceptionally high total porosity and surface area, despite having virtually no gas-accessible surface area in sorption experiments. A part of this porosity collapses upon CO_2 activation in 5092-ACC10, with the values obtained from SAXS being rather similar to those from N_2 sorption, meaning that majority of the SSA in this material is accessible. With further activation the SSA increases to approximately 2000 m^2 g^{-1} in 5092-ACC20, just as calculated by the BET model on N_2 isotherms at 77 K. Taking into account the firstly increasing and with higher degree of CO_2 activation again reducing thickness of the pore walls, l_{solid} together with the reduced I_D/I_G ratio and broader peaks in

Raman spectra, the reorganization of carbon during the progress of CO_2 activation and the related Boudouard-equilibrium is highlighted. During this course, large, closed pores in 5092-CC are transferred to an ordinary activated carbon material. The contribution of fluctuation due to lateral imperfections and crystallite size, as can be seen in Table S3, increases from 10 in 5092-CC, to 28 in ACC10, to finally 36 in ACC20 and only corroborates this model. While plasma etching has a rather low impact on contributions from fluctuation, p-C_3N_4 deposition tends to decrease this contribution, especially, if higher amounts are introduced. The p-C_3N_4 deposition leads to a smoothing-out of the imperfections (defects) as can be seen from an increase of the parameter l_R and the decrease of the degree of disorder (DoD) parameter $<\Delta^2 a_3>/<a_3>^2 + <\Delta^2 l_R>/<l_R>^2$ (SI eq. 12). Therefore, it can be concluded that the surface of the pore walls is annealed by CVD. This in turn leads to the assumption that there is an empirical correlation between the continuity of DoD and substantial distance that the electrons can move/arrange during the low potential sodium storage, which both are ensured in 5092-CC, −CC−C3N4, and −ACC10-C3N4. Kratky Plot analysis further reveals that the largest pores are found in 5092-CC (being so-called supermicroporous ($l_{pore} > 2.0$ nm) and that upon CO_2 activation the pore size and volume decrease, i.e., the samples become more ultramicroporous (Fig. 6, Table S3).

Also here it seems that the CVD has the highest impact on most activated fibers 5092-ACC20, where the average pore diameter increases and the porosity shrinks. Clearly, contrast variation experiments and data are needed to draw further conclusions in this regard. Thus, future experiments will be performed to understand the pores' connectivity and pore accessibility in Kynol fibers via contrast variation SAXS experiments combined with gas-physisorption.
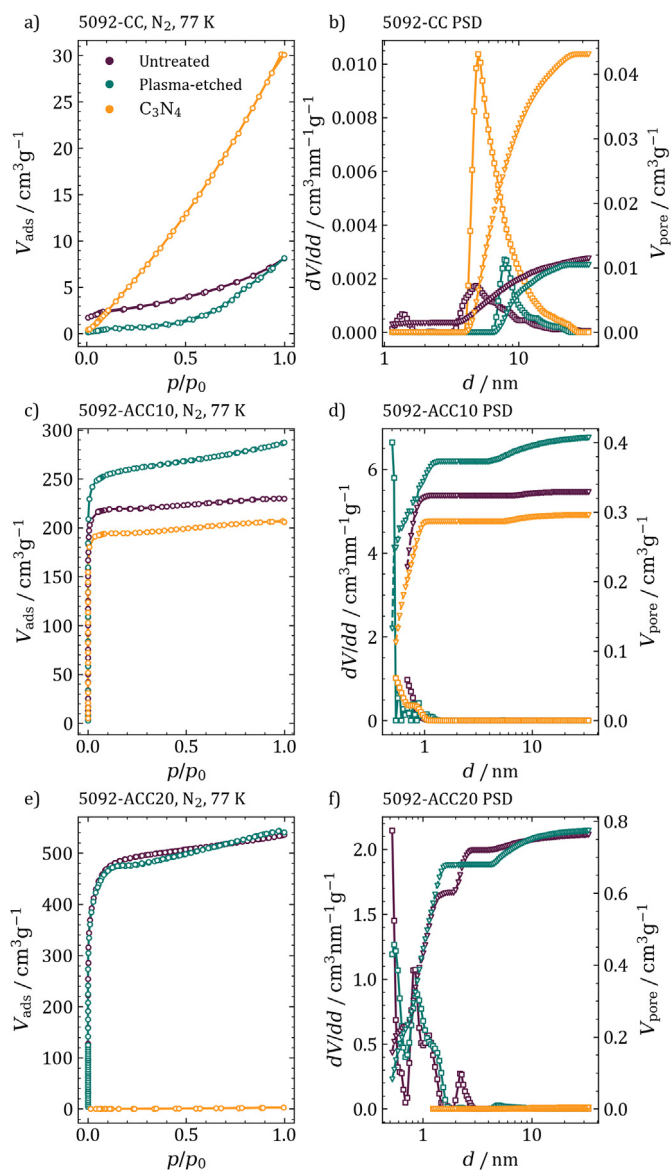
Fig. 5. a), c), e): N2 sorption isotherms of all investigated materials at 77 K. b), d), f): Pore size distributions calculated from a QSDFT kernel for slit/cylindrical pores using the adsorption branch of the isotherm. (A colour version of this figure can be viewed online.)

3.2. Electrochemical sodium storage in open and closed pores

Galvanostatic charge-discharge curves were recorded at currents as low as 18.6 mA g^{-1}, which corresponds to C/20 of a Li/graphite cell.

The results can be found in Fig. 7. As it could be expected, highly microporous carbons 5092-ACC10 and -ACC20 exhibit a high irreversible capacity in the first cycle, followed by a rather low, sloping capacity of about 40 mAh g^{-1}. After surpassing the voltage limit of 0 V, sodium metal immediately begins to plate on these materials, as it is evident from the voltage minimum in the charge-discharge curves, called "dip" henceforth [11,25,45]. This method is well suited for the investigation of closed porous materials, as contrary to the measurement until close to 0 V vs Na/Na$^+$ with a constant voltage step, sodiation mechanisms at potentials between the onset of metal plating are regarded. Closed porous carbon fibers 5092-CC, as well as their p-C$_3$N$_4$ composited pendants 5092-CC-C$_3$N$_4$ or
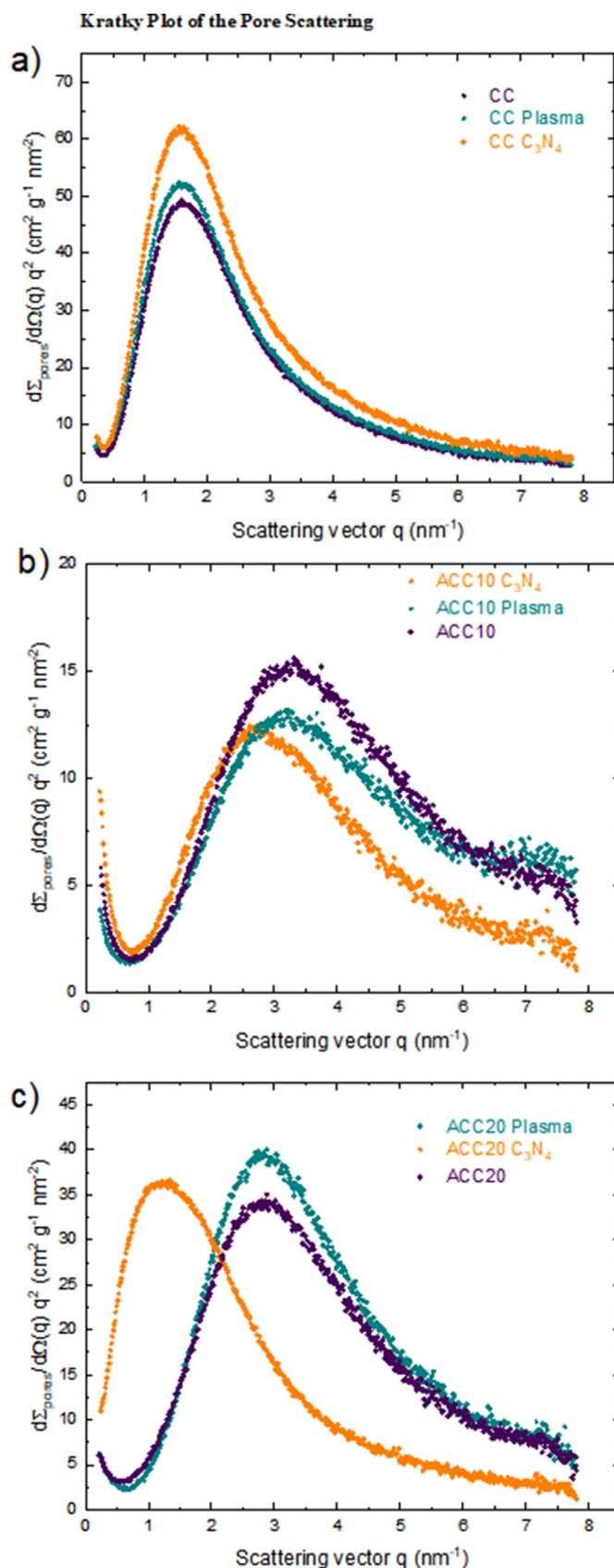

Fig. 6. Kratky plot of the pore scattering data from Fig. S7 d-f of hard carbon/carbon nitride nanocomposites powders (noted in the Figure). (A colour version of this figure can be viewed online.)
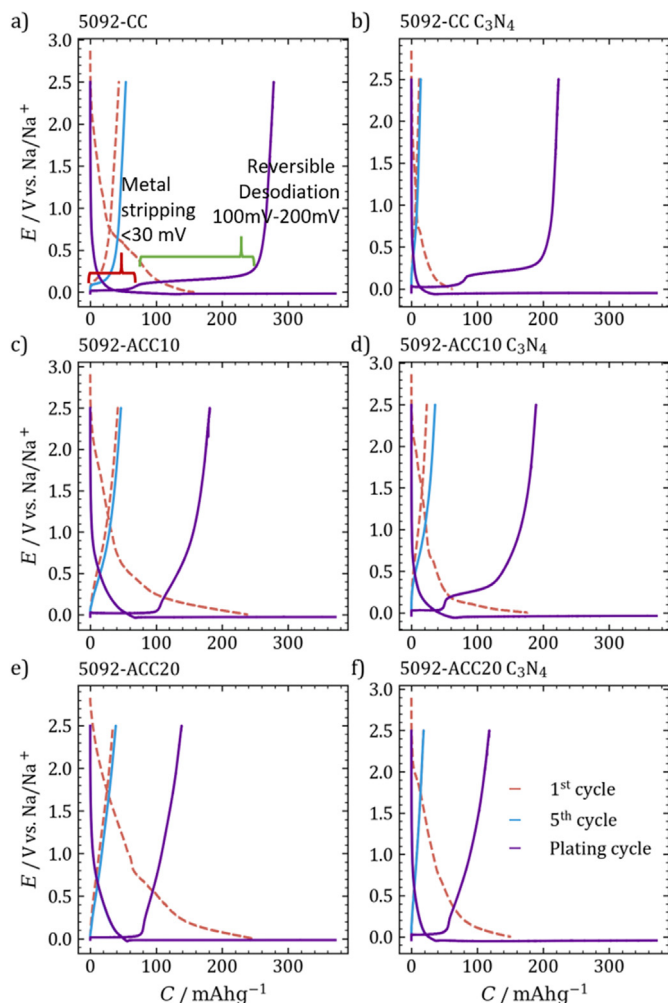
Fig. 7. Galvanostatic charge-discharge experiments recorded at 18.6 mA g^{-1} in a voltage range of 0–2.5 V for 5 cycles followed by a capacity limited cycle for the determination of the sodium metal plating capacity. (A colour version of this figure can be viewed online.)

5092-ACC10-C$_3$N$_4$ neither show any remarkable capacity above 0 V, nor does a sharp dip occur. This potential minimum usually would represent a crystallization overpotential before the onset of bulk metal plating and its absence is hence a hint that no metallic sodium is depositing at the electrode/electrolyte interface. Rather, in the desodiation cycle a voltage plateau of 174 mAh g^{-1} is measured at potentials between 100 mV and 300 mV, after excess plated sodium is partially removed from the material at a potential of 20 mV in 5092-CC. This desodiation plateau is observed only in intrinsically closed porous samples 5092-CC and 5092-CC-C$_3$N$_4$ as well as in 5092-ACC10-C$_3$N$_4$, while activated carbons as well as 5092-ACC20-C$_3$N$_4$ do not show any indication of a desodiation plateau. With the current state of SIB anode research in mind, these findings underline that closed porosity is related to low potential sodium storage, while open pores cannot be utilized as electrolyte is likely to enter them, rendering the pore volume less useful for further accommodation of quasimetallic sodium. Taking a closer look at the effect of carbon nitride addition, all the carbon/carbon nitride composites show a lower first cycle capacity, if compared to their pristine carbon counterparts. This is likely related to the significantly reduced conductivity of the nanocomposite compared to its parent carbon material, as it was determined in four-probe

conductivity measurements, summarized in Table S4. Besides the conductivity being reduced by an order of magnitude in activated carbons and a practically unchanged conductivity after plasma-etching, it is recorded that the conductivity after the CVD process is decreased by five orders of magnitude in 5092-CC, by one in 5092-ACC10 and by two in 5092-ACC20. The consequence of carbon nitride film at the surface of the fibers is not only the reduction of surface area but also a lower effective potential acting on the electrolyte molecules upon drawing an electrical current, leading to less pronounced "natural" SEI formation. The smoothing of carbon surfaces, as observed from SAXS could further contribute to the inhibition of SEI growth. It is further noticed that the sodiation process above 0 V remains nearly unchanged and proceeds via a low, sloping capacity in all the studied materials. In 5092-CC-C$_3$N$_4$ the desodiation plateau is reduced as compared to untreated 5092-CC. Interestingly, the capacity of 5092-ACC20-C$_3$N$_4$ above 0 V is reduced by a factor of 1.8, while the reversible desodiation capacity stays about the same. In general, this effect can be ascribed to the displacement of pore volume by carbon nitride apparently inactive for sodium storage and hence the increased mass of the carbon/carbon nitride composite. The most striking difference is observed between samples 5092-ACC10, and its carbon nitride coated analogue 5092-ACC10-C$_3$N$_4$. Before C$_3$N$_4$ deposition, no considerable voltage plateau is observed, neither during sodiation nor during desodiation, instead a sloping capacity as low as 49 mAh g^{-1} occurs, followed by the immediate onset of sodium metal plating. The voltage profile of 5092-ACC10-C$_3$N$_4$ is rather similar to that of untreated ACC10 above 0 V, but starts to diverge below that value, as the previously clearly present dip broadens and a desodiation plateau at approximately 300 mV appears. A total capacity of 137 ± 2 mAh g^{-1} can be therefore utilized in the nanocomposite as opposed to 76 ± 5 mAh g^{-1} in the pristine ACC10 carbon, 54 ± 6 mAh of which are found at a constant potential below 100 mV. The CVD treatment with carbon nitride enables the formation of closed pores suitable for the accommodation of quasimetallic sodium clusters. Cyclic voltammetry can help to distinguish the different processes occurring at the respective voltages. Cyclic voltammo-grams of the first cycle are shown in Fig S8 together with measurements with lower voltage limits of 0.0 and −0.1 V, respectively. In the first cycle, during which the SEI is formed, two main peaks appear in the CV curve, one at 2.1 V and one at 0.4 V [46–48]. The signals are generally smaller in all the carbon/carbon nitride nanocomposites. Further, no additional peaks occur, indicating the stability of the formed carbon nitride species in the potential range relevant for SIB anode operation.

By comparing the CV curves between 0.0 and 2.5 V and −0.1 and 2.5 V it becomes clearer, why including potentials below 0 V is of utmost importance for the full utilization of hard carbons in SIB anodes. Basically, the region between 1.0 and 2.5 V in the CV is devoid of any relevant features. A small current of about 10–20 mA g^{-1} begins to flow at potentials lower than 1 V. When approaching the value of 0 V, the current begins to increase exponentially. If the scan is reverted at 0 V, only a minor current bump is measured at 0.2 V in materials 5092-CC, −CC−C$_3$N$_4$, and −ACC10-C$_3$N$_4$, while this signal is virtually absent in the other samples. By extending the cathodic scan to −0.1 V, the exponentially increasing reductive current is continued without new features emerging. The oxidative peak at 0.2 V during the anodic peak observed in the former group of samples is however significantly higher after keeping the cell below 0 V for a prolonged time. This finding is supported by our previous work and underlines that the reversible sodium storage mechanism is arbitrarily interrupted by setting the voltage limit to 0 V and that even safe cycling is possible under capacity limited conditions, including potentials below that of metallic sodium [25]. Therefore we demonstrate the practical

viability of this extended capacity limited approach by cycling the hard carbon electrode to its reversible desodiation capacity, measured at >100 mV instead of cycling it to a negative potential limit or to a previously determined dip-capacity. An overview over the results of this experiment is presented in Fig. 8.

As opposed to commonly available hard carbons prepared by the carbonization of carbohydrates and other precursors at temperatures around 1300 °C, up to 87% of the total sodium storage capacity of Kynol 5092-CC is found at constant potentials close to 0 V vs. Na/Na^+, without a pronounced voltage slope. This is a great advantage with respect to energy density, but also when balancing such an anode, no excess mass must be introduced to account for the sloping capacity. Even if the anode is oversized in order to account for operational safety, the additional mass adds to plateau capacity and therefore again poses a benefit regarding energy density. We would also like to point out that the first cycle capacity (240 mAh g^{-1}) is comparable to the reversible desodiation capacity (222 mAh g^{-1}), see Table S5, and even when using only 90% of this capacity one encounters a capacity loss of only 15% compared to the first cycle in an unstabilized electrolyte, a value in the range of state-of-the-art hard carbons [15,17]. No deposition of metallic sodium dendrites could be observed in post-mortem analyses of cycled Kynol 5092-CC electrodes, as can be seen in Fig. S9.
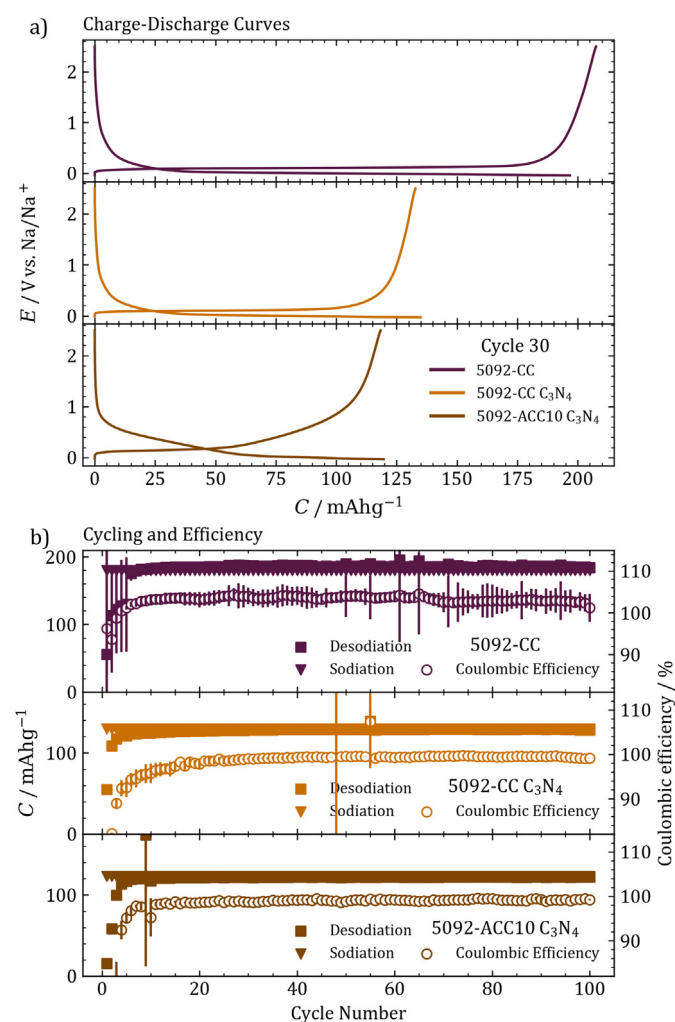

Fig. 8. Galvanostatic charge-discharge experiments recorded at 18.6 mA g^{-1} using a previously determined capacity limit for the sodiation step and 2.5 V as the desodiation limit. (A colour version of this figure can be viewed online.)

Additionally, the high coulombic efficiencies indicate against the formation of dendrites and other metallic sodium species, which is particularly impressive considering the additive-free electrolyte. These observations add some new aspects on SEI formation and full cell balancing.

Furthermore, the series allows some interesting and, in this clarity, unprecedented inferences about the structure-performance relationships on hard carbon for sodium-ion anodes. Quasimetallic sodium is stored in the abundant, rather large, closed pores present in the interior of the unactivated Kynol 5092-CC fibres at potentials close to 0 V. No clear onset of metallic sodium plating as evident from a voltage minimum is observed, because sodium enters these pores without its solvation shell solely by the mechanism of mass transfer through the solid state, and therefore can be stabilized by the carbon pore walls upon reduction. Sodium clusters with formal oxidation states near zero are formed during the reduction within closed pores. In materials with smaller closed micropores, like previously studied in our group, the size of these domains would be limited to layer coverage of the carbon surface [25]. The lack of a clear crystallization overpotential is explained by the nano-confinement of sodium clusters, rendering them amorphous if not liquid and therefore resulting in the inhibition of adopting a long range order. The nearly complete absence of sloping capacity indicates unequivocally that an adsorptive mechanism is responsible for this region of the charge-discharge curve. The structure of 5092-CC is, even if not perfectly ordered, rather poor in defects and imperfections, and instead shows non-negligible regions of graphitic stacking. Therefore, we are further able to rule out the contribution of intercalation of sodium between graphene layers to sodium storage to both, the sloping and the plateau region. This becomes even more evident, when reorganization of the material's entire closed pore structure towards an activated carbon occurs in Kynol 5092-ACC10 and -20, during which the plateau capacity fades, and a voltage slope emerges. Finally, the composite formation between porous carbon fibers and p-C_3N_4 causes significant changes in sodium storage characteristics. As can be concluded from the present data, the transformation of open to closed pores under the conditions and with the carbon materials we choose is only possible with Kynol 5092-ACC10. The key is that the small open pores in the centers of ACC10 cannot be fully reached by reactive gases in the CVD process, which is why finally the highest concentration of nitrogen is measured in the outer regions of the ACC10-C_3N_4 fiber. In contrast, a more similar concentration of nitrogen is found even in the core of the ACC20-C_3N_4 fiber. The accumulation of p-C_3N_4 forms an electrolyte-impermeable shell around the closed-porous center of ACC10-C_3N_4, while in ACC20-C_3N_4 most of the pore volume is filled with the new p-C_3N_4–phase. Building further upon these findings, one could imagine the ideal substrate for such a CVD-assisted pore closing mechanism as a hollow, thin-walled carbon particle with large micropores on the outside, with the diameter tapered towards the center. By this structure one would make sure that a dense, electrolyte- and the gas-impermeable shell would build up during CVD and the inside would remain an ideal host for storage of metallic sodium. Such a process is not only academically interesting, but it could also be at least partially adapted in practice to tune pore properties and initiate artificial SEI formation and therefore contribute to efficient sodium storage in SIB anodes.

4. Conclusion

Hard carbon/polymeric carbon nitride nanocomposite were prepared by a chemical vapor deposition approach and the impact of the substrate pore structure on the deposition dynamics and resulting sodium storage properties in SIB anodes were studied.

From thermal analysis, SEM images, as well as gas sorption experiments it could be concluded that the amount of p-C_3N_4 deposited is strongly dependent on the gas-accessible pore volume of the carbon substrate, where the reactive species in the CVD gas stream was deduced to have a diffusivity that can be set in relation to N_2 at 77 K. Therefore, substrates with larger micropores tend to be filled with p-C_3N_4 to the greatest extent, whereas samples with a pronounced fraction of ultramicropores adopt a closed porous structure surrounded by a carbon nitride phase. By means of SAXS, information about the pore structure, complementary to sorption data, was obtained. It turns out that externally non-porous Kynol 5092-CC has rather large, internal micropores delineated by thin, ordered layers of graphene and therefore can store up to 220 mAh g^{-1} of sodium, with 184 mAh g^{-1} being reversible plateau capacity. While the C_3N_4 composites all show reduced first cycle capacities compared to their pristine carbon counterparts, indicating the successful formation of an artificial p-C_3N_4 SEI, the true power of the presented method is to provide a tool to convert open porosity into a closed one, enabling sodium storage at constant, low voltages. As the majority of gas-accessible pores is located on the outward facing layers of the carbon fiber, the smaller, inaccessible layers in the center remain void and can serve as stabilizing structures for the formation of quasimetallic sodium clusters. Optimizing both, the CVD and pre-treatment conditions it is therefore possible to achieve stable and effective artificial SEIs. By further designing a tailored substrate, with large hollow structures in the inside and smaller, tapered micropores on the outward layers, the reversible formation of metallic sodium domains of controllable size and therefore high-capacity anodes becomes a realistic and practically applicable scenario for next generation SIB anodes.

In order to be able to coat powder-shaped materials, for example biomass-derived ones, which is rather the standard appearance of hard carbon anode materials, the CVD coating method should be extended and investigated using a rotating-tube CVD furnace.

The investigation of materials with artificially closed pores should be also studied at higher current densities in the future, as under conditions of higher loads effects such as polarization could begin to play a role, leading to an earlier onset of sodium metal plating. This could be performed already on more optimized materials. In this respect, in-situ spectroscopic proof of both, the presence of quasimetallic clusters, as well as the absence of metallic dendrite is necessary and should be performed in the future [49].

CRediT authorship contribution statement

Konstantin Schutjajew: Investigation, Methodology, Writing – original draft. **Paolo Giusto:** Investigation, Methodology. **Eneli Härk:** Investigation. **Martin Oschatz:** Conceptualization, Supervision, Writing – review & editing, Funding acquisition.

Declaration of competing interest

The authors declare that they have no known competing financial interests or personal relationships that could have appeared to influence the work reported in this paper.

Acknowledgements

Appendix A. Supplementary data

Supplementary data to this article can be found online at https://doi.org/10.1016/j.carbon.2021.09.051.

References

[1] Z. Yang, J. Zhang, M.C.W. Kintner-Meyer, X. Lu, D. Choi, J.P. Lemmon, J. Liu, Electrochemical energy storage for green grid, Chem. Rev. 111 (2011) 3577–3613, https://doi.org/10.1021/cr100290v.

[2] D. Larcher, J.M. Tarascon, Towards greener and more sustainable batteries for electrical energy storage, Nat. Chem. 7 (2015) 19–29, https://doi.org/10.1038/nchem.2085.

[3] N. Yabuuchi, K. Kubota, M. Dahbi, S. Komaba, Research development on sodium-ion batteries, Chem. Rev. 114 (2014) 11636–11682, https://doi.org/10.1021/cr500192f.

[4] B. Jache, P. Adelhelm, Use of graphite as a highly reversible electrode with superior cycle life for sodium-ion batteries by making use of co-intercalation phenomena, Angew. Chem. Int. Ed. 53 (2014) 10169–10173, https://doi.org/10.1002/anie.201403734.

[5] Y. Nishi, The development of lithium ion secondary batteries, Chem. Rec. 1 (2001) 406–413, https://doi.org/10.1002/tcr.1024.

[6] A. Yoshino, The birth of the lithium-ion battery, Angew. Chem. Int. Ed. 51 (2012) 5798–5800, https://doi.org/10.1002/anie.201105006.

[7] D. Saurel, J. Segalini, M. Jauregui, A. Pendashteh, B. Daffos, P. Simon, M. Casas-Cabanas, A SAXS outlook on disordered carbonaceous materials for electrochemical energy storage, Energy Storage Mater 21 (2019) 162–173, https://doi.org/10.1016/j.ensm.2019.05.007.

[8] X. Dou, I. Hasa, D. Saurel, C. Vaalma, L. Wu, D. Buchholz, D. Bresser, S. Komaba, S. Passerini, Hard carbons for sodium-ion batteries: structure, analysis, sustainability, and electrochemistry, Mater. Today 23 (2019) 87–104, https://doi.org/10.1016/j.mattod.2018.12.040.

[9] R.E. Franklin, The structure of graphitic carbons, Acta Crystallogr. 4 (1951) 253–261, https://doi.org/10.1107/s0365110x51000842.

[10] D.A. Stevens, J.R. Dahn, An in situ small-angle X-ray scattering study of sodium insertion into a nanoporous carbon anode material within an operating electrochemical cell, J. Electrochem. Soc. 147 (2000) 4428, https://doi.org/10.1149/1.1394081.

[11] Y. Morikawa, S. ichi Nishimura, R. ichi Hashimoto, M. Ohnuma, A. Yamada, Mechanism of sodium storage in hard carbon: an X-ray scattering analysis, Adv. Energy Mater. 10 (2020) 1–9, https://doi.org/10.1002/aenm.201903176.

[12] J.M. Stratford, P.K. Allan, O. Pecher, P.A. Chater, C.P. Grey, Mechanistic insights into sodium storage in hard carbon anodes using local structure probes, Chem. Commun. 52 (2016) 12430–12433, https://doi.org/10.1039/c6cc06990h.

[13] R. Morita, K. Gotoh, M. Fukunishi, K. Kubota, S. Komaba, N. Nishimura, T. Yumura, K. Deguchi, S. Ohki, T. Shimizu, H. Ishida, Combination of solid state NMR and DFT calculation to elucidate the state of sodium in hard carbon electrodes, J. Mater. Chem. A. 4 (2016) 13183–13193, https://doi.org/10.1039/c6ta04273b.

[14] K. Gotoh, T. Yamakami, I. Nishimura, H. Kometani, H. Ando, K. Hashi, T. Shimizu, H. Ishida, Mechanisms for overcharging of carbon electrodes in lithium-ion/sodium-ion batteries analysed by operando solid-state NMR, J. Mater. Chem. A. 8 (2020) 14472–14481, https://doi.org/10.1039/D0TA04005C.

[15] D. Saurel, B. Orayech, B. Xiao, D. Carriazo, X. Li, T. Rojo, From charge storage mechanism to performance: a roadmap toward high specific energy sodium-ion batteries through carbon anode optimization, Adv. Energy Mater. 8 (2018) 1703268, https://doi.org/10.1002/aenm.201703268.

[16] F. Xu, H. Han, Y. Qiu, E. Zhang, H. Repich, C. Qu, H. Yu, H. Wang, S. Kaskel, Facile regulation of carbon framework from the microporous to low-porous via molecular crosslinker design and enhanced Na storage, Carbon N. Y. 167 (2020) 896–905, https://doi.org/10.1016/j.carbon.2020.05.081.

[17] A. Kamiyama, K. Kubota, D. Igarashi, Y. Youn, Y. Tateyama, H. Ando, K. Gotoh, S. Komaba, MgO-template synthesis of extremely high capacity hard carbon for Na-ion battery, Angew. Chem. Int. Ed. (2020) 1–8, https://doi.org/10.1002/anie.202013951.

[18] Y. Wang, X. Wang, M. Antonietti, Polymeric graphitic carbon nitride as a heterogeneous organocatalyst: from photochemistry to multipurpose catalysis to sustainable chemistry, Angew. Chem. Int. Ed. 51 (2012) 68–89, https://doi.org/10.1002/anie.201101182.

[19] A. Thomas, A. Fischer, F. Goettmann, M. Antonietti, J.-O. Müller, R. Schlögl, J.M. Carlsson, Graphitic carbon nitride materials: variation of structure and morphology and their use as metal-free catalysts, J. Mater. Chem. 18 (2008) 4893, https://doi.org/10.1039/b800274f.

[20] P. Giusto, D. Cruz, T. Heil, H. Arazoe, P. Lova, T. Aida, D. Comoretto, M. Patrini, M. Antonietti, Shine bright like a diamond: new light on an old polymeric semiconductor, Adv. Mater. 32 (2020) 1908140, https://doi.org/10.1002/adma.201908140.

[21] P. Giusto, B. Kumru, J. Zhang, R. Rothe, M. Antonietti, Let a Hundred Polymers Bloom: Tunable Wetting of Photografted Polymer-Carbon Nitride Surfaces, 2020, https://doi.org/10.1021/acs.chemmater.0c01798.

[22] G.Y. Gor, M. Thommes, K.A. Cychosz, A.V. Neimark, Quenched solid density functional theory method for characterization of mesoporous carbons by nitrogen adsorption, Carbon N. Y. 50 (2012) 1583–1590, https://doi.org/10.1016/j.carbon.2011.11.037.

[23] J. Silvestre-Albero, A. Silvestre-Albero, F. Rodríguez-Reinoso, M. Thommes, Physical characterization of activated carbons with narrow microporosity by nitrogen (77.4 K), carbon dioxide (273 K) and argon (87.3 K) adsorption in combination with immersion calorimetry, Carbon N. Y. 50 (2012) 3128–3133, https://doi.org/10.1016/j.carbon.2011.09.005.

[24] C.A. Dreiss, K.S. Jack, A.P. Parker, On the absolute calibration of bench-top small-angle X-ray scattering instruments: a comparison of different standard methods, J. Appl. Crystallogr. 39 (2006) 32–38, https://doi.org/10.1107/S0021889805033091.

[25] K. Schutjajew, J. Pampel, W. Zhang, M. Antonietti, M. Oschatz, Influence of pore architecture and chemical structure on the sodium storage in nitrogen-doped hard carbons, Small (2021) 2006767, https://doi.org/10.1002/smll.202006767.

[26] J.R. Dahn, T. Zheng, Y. Liu, J.S. Xue, Mechanisms for lithium insertion in carbonaceous materials, Science (80-.) 270 (1995) 590–593, https://doi.org/10.1126/science.270.5236.590.

[27] K. Kubota, S. Shimadzu, N. Yabuuchi, S. Tominaka, S. Shiraishi, M. Abreu-Sepulveda, A. Manivannan, K. Gotoh, M. Fukunishi, M. Dahbi, S. Komaba, Structural analysis of sucrose-derived hard carbon and correlation with the electrochemical properties for lithium, sodium, and potassium insertion, Chem. Mater. 32 (2020) 2961–2977, https://doi.org/10.1021/acs.chemmater.9b05235.

[28] A.B. García, A. Martínez-Alonso, C.A. Leon Y Leon, J.M.D. Tascón, Modification of the surface properties of an activated carbon by oxygen plasma treatment, Fuel 77 (1998) 613–624, https://doi.org/10.1016/S0016-2361(97)00111-7.

[29] A.C. Ferrari, J. Robertson, Interpretation of Raman spectra of disordered and amorphous carbon, Phys. Rev. B 61 (2000) 14095–14107, https://doi.org/10.1103/PhysRevB.61.14095.

[30] A.C. Ferrari, J. Robertson, Resonant Raman spectroscopy of disordered, amorphous, and diamondlike carbon, Phys. Rev. B Condens. Matter 64 (2001) 1–13, https://doi.org/10.1103/PhysRevB.64.075414.

[31] C. Hu, S. Sedghi, A. Silvestre-Albero, G.G. Andersson, A. Sharma, P. Pendleton, F. Rodríguez-Reinoso, K. Kaneko, M.J. Biggs, Raman spectroscopy study of the transformation of the carbonaceous skeleton of a polymer-based nanoporous carbon along the thermal annealing pathway, Carbon N. Y. 85 (2015) 147–158, https://doi.org/10.1016/j.carbon.2014.12.098.

[32] A.C. Forse, C. Merlet, P.K. Allan, E.K. Humphreys, J.M. Griffin, M. Aslan, M. Zeiger, V. Presser, Y. Gogotsi, C.P. Grey, New insights into the structure of nanoporous carbons from NMR, Raman, and pair distribution function analysis, Chem. Mater. 27 (2015) 6848–6857, https://doi.org/10.1021/acs.chemmater.5b03216.

[33] M.W. Smith, I. Dallmeyer, T.J. Johnson, C.S. Brauer, J.S. McEwen, J.F. Espinal, M. Garcia-Perez, Structural analysis of char by Raman spectroscopy: improving band assignments through computational calculations from first principles, Carbon N. Y. 100 (2016) 678–692, https://doi.org/10.1016/j.carbon.2016.01.031.

[34] M. Pawlyta, J.N. Rouzaud, S. Duber, Raman microspectroscopy characterization of carbon blacks: spectral analysis and structural information, Carbon N. Y. 84 (2015) 479–490, https://doi.org/10.1016/j.carbon.2014.12.030.

[35] Z.Y. Chen, J.P. Zhao, T. Yano, T. Ooie, Raman characteristics of carbon nitride synthesized by nitrogen-ion-beam-assisted pulsed laser deposition, Appl. Phys. Mater. Sci. Process 74 (2002) 213–216, https://doi.org/10.1007/s003390100859.

[36] S.E. Rodil, A.C. Ferrari, J. Robertson, W.I. Milne, Raman and infrared modes of hydrogenated amorphous carbon nitride, J. Appl. Phys. 89 (2001) 5425–5430, https://doi.org/10.1063/1.1365076.

[37] M. Thommes, K. Kaneko, A.V. Neimark, J.P. Olivier, F. Rodriguez-Reinoso, J. Rouquerol, K.S.W. Sing, Physisorption of gases, with special reference to the evaluation of surface area and pore size distribution (IUPAC Technical Report), Pure Appl. Chem. 87 (2015) 1051–1069, https://doi.org/10.1515/pac-2014-1117.

[38] J. Mering, C. Schiller, Diffusion centrale des rayons X par des carbones graphitables. Déviation de la loi de Porod, Comptes Rendus l'Académie Des Sci. (1967) 247–250.

[39] R. Perret, W. Ruland, X-ray small-angle scattering of non-graphitizable carbons, J. Appl. Crystallogr. 1 (1968) 308–313, https://doi.org/10.1107/s0021889868005558.

[40] R. Perret, W. Ruland, X-ray small-angle scattering of glassy carbon, J. Appl. Crystallogr. 5 (1972) 183–187, https://doi.org/10.1107/s0021889872009161.

[41] W. Ruland, Carbon fibers, Adv. Mater. 2 (1990) 528–536, https://doi.org/10.1002/adma.19900021104.

[42] W. Ruland, Apparent fractal dimensions obtained from small-angle scattering of carbon materials, Carbon N. Y. 39 (2001) 323–324, https://doi.org/10.1016/S0008-6223(00)00256-6.

[43] C.J. Jafta, A. Petzold, S. Risse, D. Clemens, D. Wallacher, M. Goerigk, M. Ballauff, Correlating pore size and shape to local disorder in microporous carbon: a combined small angle neutron and X-ray scattering study, Carbon N. Y. 123 (2017) 440–447, https://doi.org/10.1016/j.carbon.2017.07.046.

[44] E. Härk, A. Petzold, G. Goerigk, S. Risse, I. Tallo, R. Härmas, E. Lust, M. Ballauff, Carbide derived carbons investigated by small angle X-ray scattering: inner surface and porosity vs. graphitization, Carbon N. Y. 146 (2019) 284–292, https://doi.org/10.1016/j.carbon.2019.01.076.

[45] Y. Zheng, Y. Lu, X. Qi, Y. Wang, L. Mu, Y. Li, Q. Ma, J. Li, Y.S. Hu, Superior electrochemical performance of sodium-ion full-cell using poplar wood derived hard carbon anode, Energy Storage Mater 18 (2019) 269–279, https://doi.org/10.1016/j.ensm.2018.09.002.

[46] G.G. Eshetu, S. Grugeon, H. Kim, S. Jeong, L. Wu, G. Gachot, S. Laruelle, M. Armand, S. Passerini, Comprehensive insights into the reactivity of electrolytes based on sodium ions, ChemSusChem 9 (2016) 462–471, https://doi.org/10.1002/cssc.201501605.

[47] I.A. Shkrob, Y. Zhu, T.W. Marin, D. Abraham, Reduction of carbonate electrolytes and the formation of solid-electrolyte interface (SEI) in lithium-ion batteries. 1. Spectroscopic observations of radical intermediates generated in one-electron reduction of carbonates, J. Phys. Chem. C 117 (2013) 19255–19269, https://doi.org/10.1021/jp406274e.

[48] C. Peschel, F. Horsthemke, M. Leißing, S. Wiemers-Meyer, J. Henschel, M. Winter, S. Nowak, Analysis of carbonate decomposition during solid electrolyte interphase formation in isotope-labeled lithium ion battery electrolytes: extending the knowledge about electrolyte soluble species, Batter. Supercaps. 3 (2020) 1183–1192, https://doi.org/10.1002/batt.202000170.

[49] P.M. Bayley, N.M. Trease, C.P. Grey, Insights into electrochemical sodium metal deposition as probed with in Situ ^{23}Na NMR, J. Am. Chem. Soc. 138 (2016) 1955–1961, https://doi.org/10.1021/jacs.5b12423.